

Single-Molecule Junction Origami

Chuanli Wu, Demetris Bates, Sara Sangtarash, Nicolò Ferri, Aidan Thomas, [Simon Higgins](#), Craig M. Robertson, Richard Nichols, Hatf Sadeghi, [Andrea Vezzoli](#)

Submitted date: 01/05/2020 • Posted date: 05/05/2020

Licence: CC BY-NC-ND 4.0

Citation information: Wu, Chuanli; Bates, Demetris; Sangtarash, Sara; Ferri, Nicolò; Thomas, Aidan; Higgins, Simon; et al. (2020): Single-Molecule Junction Origami. ChemRxiv. Preprint.

<https://doi.org/10.26434/chemrxiv.12229202.v1>

Stimuli-responsive molecular junctions, where the conductance can be altered by an external perturbation, are an important class of nanoelectronic devices. These have recently attracted interest as large effects can be introduced through exploitation of quantum phenomena. We show here that significant changes in conductance can be attained as a molecule is repeatedly compressed and relaxed, resulting in molecular folding along a flexible fragment and cycling between an anti and a syn conformation. Power spectral density analysis and DFT transport calculations show that through-space tunnelling between two phenyl fragments is responsible for the conductance increase as the molecule is mechanically folded to the syn conformation. This phenomenon represents a novel class of mechanoresistive molecular devices, where the functional moiety is embedded in the conductive backbone and exploits intramolecular nonbonding interactions, in contrast to most studies where mechanoresistivity arises from changes in the molecule-electrode interface.

File list (3)

Wu_DKDTSwitch.pdf (1.44 MiB)

[view on ChemRxiv](#) • [download file](#)

Wu_DKDTSwitch_TOC.png (514.71 KiB)

[view on ChemRxiv](#) • [download file](#)

Wu_DKDTSwitch_SI.pdf (2.47 MiB)

[view on ChemRxiv](#) • [download file](#)

Single-Molecule Junction Origami[†]

Chuanli Wu[‡], Demetris Bates[‡], Sara Sangtarash[‡], Nicolás Ferri, Aidan Thomas, Simon J. Higgins, Craig M. Robertson, Richard J. Nichols, Hatef Sadeghi* and Andrea Vezzoli*

[†] Ms. Chuanli Wu, Mr. Demetris Bates, Dr. Nicolás Ferri, Mr. Aidan Thomas, Dr. Craig M. Robertson, Prof. Dr. Simon J. Higgins, Prof. Dr. Richard J. Nichols and Dr. Andrea Vezzoli
Department of Chemistry, University of Liverpool, Crown Street, Liverpool L69 7ZD, United Kingdom
e-mail for Dr. Andrea Vezzoli: andrea.vezzoli@liverpool.ac.uk

Ms. Chuanli Wu
School of Chemistry and Materials Science, Nanjing Normal University, Nanjing 210023, People's Republic of China

Dr. Sara Sangtarash and Dr. Hatef Sadeghi
School of Engineering, University of Warwick, Coventry CV4 7AL, U.K.
e-mail for Dr. Hatef Sadeghi: hatef.sadeghi@warwick.ac.uk

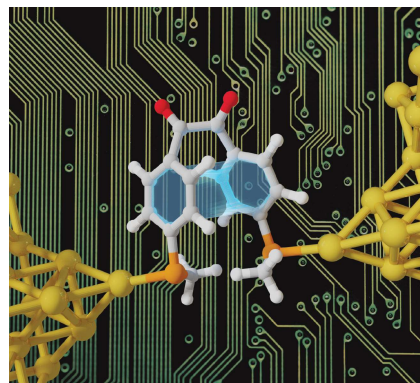
Dr. Andrea Vezzoli
Stephenson Institute for Renewable Energy, University of Liverpool, Peach Street, Liverpool L69 7ZF, United Kingdom

[‡]: these authors contributed equally to this work.

* corresponding authors: andrea.vezzoli@liverpool.ac.uk
hatef.sadeghi@warwick.ac.uk

Abstract

Stimuli-responsive molecular junctions, where the conductance can be altered by an external perturbation, are an important class of nanoelectronic devices. These have recently attracted interest as large effects can be introduced through exploitation of quantum phenomena. We show here that significant changes in conductance can be attained as a molecule is repeatedly compressed and relaxed, resulting in molecular folding along a flexible fragment and cycling between an *anti* and a *syn* conformation. Power spectral density analysis and DFT transport calculations show that through-space tunnelling between two phenyl fragments is responsible for the conductance increase as the molecule is mechanically folded to the *syn* conformation. This phenomenon represents a novel class of mechanoresistive molecular devices, where the functional moiety is embedded in the conductive backbone and exploits intramolecular nonbonding interactions, in contrast to most studies where mechanoresistivity arises from changes in the molecule-electrode interface.



Main Text

Apart from fundamental studies focussing on archetypal saturated compounds such as α, ω -alkanedithiols^[1–3] and α, ω -alkanediamines,^[4–6] the majority of molecular wires employed to fabricate molecular junctions are rod-like, π -conjugated structures. They have found such a widespread use because their extensive conjugation results in high conductance, and the conformationally rigid π -system avoids complications which could arise, for instance, from *gauche* defects in saturated carbon chains.^[7,8] Controlled conformational flexibility, however, can be used to impart functionality. Franco *et al.* proposed a theoretical exploitation of flexible fragments in single-molecule junctions to develop force-sensitive single-molecule devices,^[9] based on π -stacking perylene units linked by a saturated propyl chain, that would “unstack” as the junction is stretched. Stacks of phenyl rings and other simple heteroaromatics are able to act as efficient conductors in molecular junctions,^[10,11] with charge transported through π - π interactions.^[12–17] As the stacking configuration is unfolded, conductance is predicted to drop by orders of magnitude, as tunnelling through a saturated propyl chain is very inefficient. Such a device would represent a new class of molecular electronic devices responsive to mechanical stimuli, complementing the existing range that exploits changes in the electrode-molecule interface,^[18–24] stereoelectronic configuration switching,^[25] and stretching-dependent quantum interference effects^[12,26] as the molecular junction is compressed and relaxed.

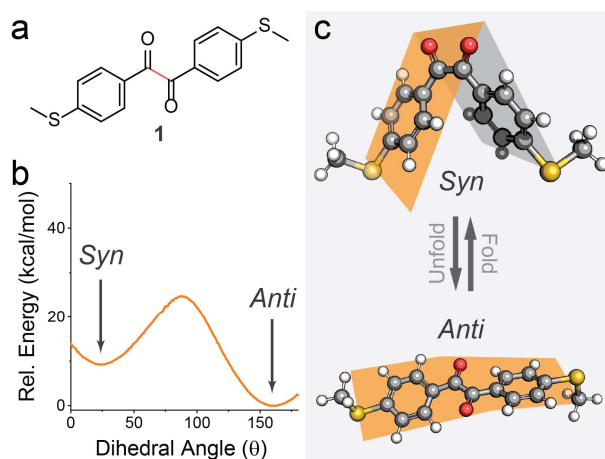


Figure 1: Molecular Design. a) structure of compound **1** with the conformationally flexible bond highlighted in orange. b) Energy vs. O=C-C=O dihedral angle for compound **1** obtained by MM2 Force Field calculations. c) 3D structures of **1** in the *anti* (dihedral of 155°) and *syn* (dihedral of 23°) conformations.

Intrigued by these phenomena, we designed molecule **1** to have two phenyl rings spaced by a diketone chain. The molecule has a conformationally flexible bond between the two sp^2 -hybridised carbonyls (orange in Figure 1a). While the ground state structure is a *quasi-anti* conformation, similar to benzil (an analogue of **1** without the thiomethyl termini),^[27] the central C-C bond in such compounds has a dihedral torsional barrier of only 15 – 45 kJ/mol (0.15 –

0.5 eV) for interconversion between the *syn* and *anti* conformations.^[28,29] We performed simple molecular mechanics calculations (MM2 Force Field) on **1** to obtain the ground state energy as a function of the (C=O)-(C=O) dihedral angle θ . We found that the energy profile has two minima, with approximately 130° of difference between them (Figure 1) and shallow energy barriers. Our results suggest that a *syn* ($\theta < 90^\circ$) \rightleftharpoons *anti* ($\theta > 90^\circ$) conversion should be readily attained by compressing a metal-molecule-metal junction made with **1** and *mechanically folding* the molecule along the central C–C bond. π – π interactions between the two phenyl rings in the *syn* conformer would then contribute significantly to charge transport (in a way akin to π -stacking), allowing us to detect the interconversion by measuring the junction conductance.

We therefore synthesized **1** and used the scanning tunnelling microscope – break junction technique (*STM-BJ*)^[1] to fabricate its molecular junctions and measure their conductance. In this method, Au point contacts having conductance $G = G_0 \cong 77.48 \mu S$ are repeatedly fabricated and ruptured by driving an atomically sharp Au wire into and out of contact with a Au on mica substrate. When the process is performed in a solution of a suitable molecular wire, molecular junctions self-assemble in the freshly ruptured point contact, and molecular charge transport can be determined as a function of electrode separation. The process is repeated thousands of times under DC bias voltage V , while recording the current I as a function of the electrode displacement z . Conductance is calculated as $G = I/V$ and the obtained G_z traces are compiled into 1D histograms and 2D density maps yielding, respectively, the distribution of conductance values, and the correlation of junction conductance and junction size.

We performed the process in a 1 mM mesitylene solution of **1**, and the results can be observed in Figure 2. The conductance histogram (Figure 2b) shows two main contributions: a high-conductance ($\sim 10^{-3} G_0$) feature, at small junction size (~ 0.8 nm, accounting for the electrodes snapback^[18]), and a low conductance feature ($\sim 10^{-4} G_0$) at larger junction size (~ 1.2 nm including snapback). The results therefore suggest the presence of two possible conformers of **1** in the junction, with conductance difference of more than one order of magnitude and a difference in size of 0.4 nm. We then performed piezo-modulation experiments on the fabricated junctions. In these experiments, nanogaps able to accommodate the extended *anti* conformation (1.2 nm) are initially fabricated, and their size is then modulated by applying a square wave signal to the piezo voltage. The molecule is therefore allowed to assemble in the gap in its thermodynamically favoured *anti* state, and it is then mechanically folded into the *syn* conformation by compressing the junction. More information on the piezo-modulation experiments can be found in our previous publications on the subject^[19,20] and details are

provided in the SI. Under a modulation amplitude of 0.4 nm the junctions could be cycled reliably from the high- G to the low- G conformation, with excellent repeatability (Figure 2d).

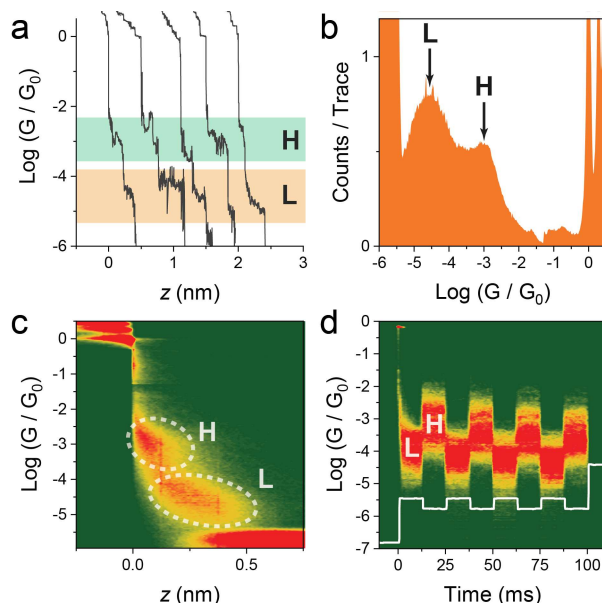


Figure 2: *STM-BJ* Data. a) example G_z traces for **1** under constant electrode displacement speed (20 nm / s). b) conductance histogram for **1** compiled with 7678 traces as shown in (a) with no data selection. c) Conductance – electrode displacement density map of **1**. d) Density map of piezo-modulation experiments. After an abrupt 1.2 nm stretch that opens the nanogap, the junction size is compressed by 0.4 nm and then relaxed again, for four times in 100 ms. The piezo signal is superimposed as a grey line for clarity. Histograms and 2D maps compiled with 100 bins / decade, 100 bins / nm and 1000 bins / second. Experiments performed at 200 mV tip-substrate bias.

We can rule out any contributions from variations in the molecule-electrode interface as a mechanism for the observed switching phenomena, as we have already demonstrated that thioanisole contacts do not change binding configuration upon junction compression.^[20] Similarly, we can discount an interpretation of our results based on the formation of shorter junctions through Au-carbonyl contacts, as no interactions between a (di)ketone and gold electrodes (e.g. in measurements of molecular wires containing fluorenones,^[30] anthraquinones^[31] or diketopyrrolopyrroles^[32]) have been reported. To verify that a *syn* \rightleftharpoons *anti* conformation change is responsible for the observed mechanoresistive effects, we performed power spectral density (PSD) analysis^[33] on the junctions in their relaxed and compressed state. PSD has been used in the literature to characterize through-space coupling in molecular junctions where charge transport does not follow the chemical bond organization, but travels through eigenchannels opened by non-bonding interactions.^[13,14,34,35] When charge transport is purely through-bond, the *Noise Power* (the integral of the power spectral density) scales approximately with G , while the scaling increases when charge transport has a through-space character, to approach the value found for pure through-space tunnelling of G^2 . When *Noise Power* is normalized by the average conductance G_{AVG} (*Noise Power*/ G_{AVG}) it is therefore generally found to be insensitive to the junction conductance for through-bond

coupling. On the other hand, a strong correlation between $Noise\ Power/G_{AVG}$ and G_{AVG} is observed when through-space coupling significantly contributes to charge transport.^[33] In order to estimate $Noise\ Power/G_{AVG}$ we performed modulation experiments by fabricating junctions in their relaxed state, recording the current for 50 ms, then compressing them by 0.4 nm and recording the current for another 50 ms (Figure 3a). Slices of data (30 ms) in the relaxed and stretched state are then analysed with a Fast Fourier Transform (FFT) algorithm to obtain the PSD, which is numerically integrated between 100 Hz and 1 kHz to yield the $Noise\ Power$ in the region of interest. Normalization by the calculated average conductance of the junction yields $Noise\ Power/G_{AVG}$ which is plotted versus G_{AVG} to examine their correlation. More information about the data collection and analysis process can be found in the SI.

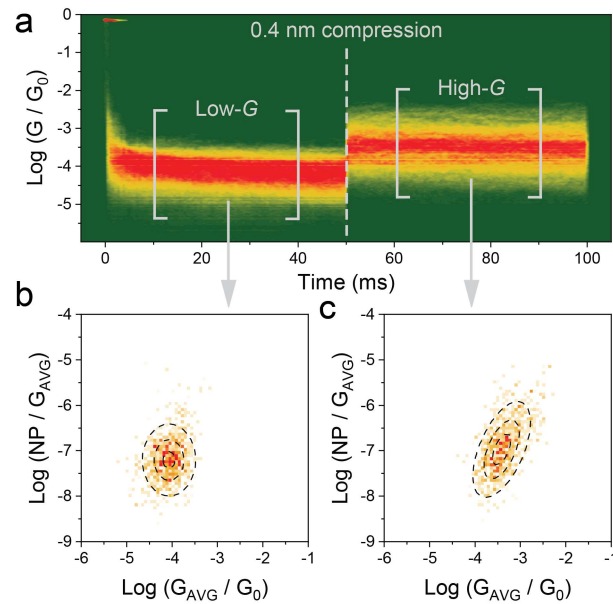


Figure 3: PSD analysis. a) Conductance vs time density map for a single compression cycle of **1**. The portions between brackets were then cut off and analysed with a FFT algorithm to calculate the *Noise Power*. b) Normalised *Noise Power* vs G_{AVG} heatmap for **1** in the low- G , relaxed junction state. c) Normalised *Noise Power* vs G_{AVG} heatmap for **1** in the high- G , compressed junction state. Data compiled from 8214 traces. 2D map in (a) compiled with 100 bins / decade and 2000 bins / second. Heatmaps in (b) and (c) compiled with 15 bins per decade. The dashed lines in panels (b) and (c) are the 25, 50 and 75% height contours of a 2D gaussian surface fitted to the experimental data. All experiments performed at 200 mV tip-substrate bias.

Junctions in their relaxed, low- G state showed *Noise Power* insensitive to conductance, thus confirming a dominant through-bond mechanism of charge transport (Figure 3b). In the compressed, high- G state, however, *Noise Power* strongly correlates with the average conductance of the junction (Figure 3c), indicating that through-space tunnelling phenomena are now contributing to the overall charge transport. This further reinforces our proposed interpretation of a mechanoresistive behaviour arising from conformational change, where a non-bonding transport channel is opened upon folding the junction to the *syn* conformation.

As a further control experiment, we studied the (*E*)-stilbene analogue of **1** ((*E*)-1,2-bis(4-(methylthio)phenyl)ethene, see SI), which the central C=C bond renders conformationally locked. We found no evidence of mechanically-controlled conductance switching in the STM-BJ and piezo-modulation experiments, showing that (i) a conformationally flexible molecule is needed to attain the switching behaviour and (ii) direct electrode-electrode tunnelling does not contribute significantly to the overall charge transport with the piezo ramps used in this study. Furthermore, PSD analysis suggests a purely through-bond charge transport mechanism ($Noise\ Power/G_{AVG}$ insensitive to G_{AVG}). Details on these control experiments can be found in the SI. Our results may also provide a novel explanation for high-conductance features at short junction extensions, which have been seen in similar foldable molecules incorporating two phenyl rings such as MeS-C₆H₄-Q-Q-Q-C₆H₄-SMe (Q = CH₂, SiMe₂, GeMe₂).^[36,37] It is worth noting that the prominence of the high conductance feature is significantly greater in our data compared to these systems, where it only appears as a weak peak in the histograms. We attribute this increased prominence to the sp² hybridization of the diketone bridge of **1** (in contrast with the -Q-Q-Q- sp³ hybridization), that results in a preferential rotation around the (O=C)-(C=O) axis and a more efficient folding of the junction, which is also energetically favoured by the relatively long C-C bond (1.54 Å in the solid-state crystal structure of **1**).

We then performed density functional theory (DFT) quantum transport calculations on the junction in the relaxed and extended states, by imposing constraints on the distance between the two metallic electrodes and letting the molecular portion of the junction relax to its energy minimum. Our calculations show that the molecule is indeed likely to adopt a *syn* conformation upon junction compression (Figure 4a). DFT modelling predicts a total energy difference between the *anti* and the *syn* conformation of 0.42 eV. This is less than the binding energy between the molecule and the two Au electrodes (0.54 eV) and we therefore expect the molecule to fold around the conformationally flexible C–C bond as the junction is compressed. The Gollum code^[38] was then used to calculate the transmission coefficient $T(E)$ for electrons of energy E passing from the source to the drain electrode of the junction, through molecule **1**. The electrical conductance then can be obtained using the Landauer formula, and we analysed the whole behaviour of $T(E)$ within the HOMO-LUMO gap (see methods in the SI). Transport calculations on the two states (Figure 4b) show that the value of $T(E)$ is indeed strongly dependent on electrode compression. Our calculations show that for the whole energy range between the HOMO and LUMO, $T(E)$ is lower for the *anti* conformation compared to the *syn* conformation (calculated by constraining the junction size to ~0.8 nm). $T(E)$ is raised by more than one order of magnitude in the compressed state (see grey region in Fig. 4b), in good agreement with the experimental results.

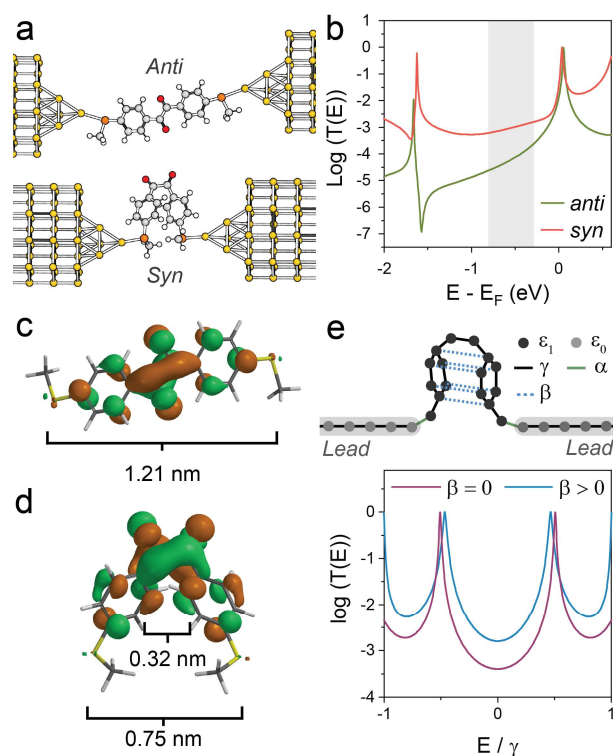


Figure 4: Theoretical Calculations. a) Structure of the junctions obtained by DFT and used for the transport calculations. b) $T(E)$ curves for compound **1** in the relaxed (*anti*) and compressed (*syn*) junction conformations. The grey shaded area represents the range of energy values where there is good agreement with the experimental data. c) LUMO of **1** in its relaxed, *anti* state. d) LUMO of **1** when a constraint is imposed on the S...S distance, and the molecule adopts a *syn* conformation. e) Tight-binding model for **1** in the *syn* configuration, with $\varepsilon_0 = \varepsilon_1 = 0$, $\gamma = -1$ and $\alpha = -0.2$. The ω B97X-D functional, 6-31G* basis set and an isovalue of 0.03 was used to produce panels (c) and (d).

Analysis of the LUMO isosurface of the two conformers (Figure 4c and 4d) shows that two lobes of opposite sign are brought within short distance as the junction is compressed, as the bonds on which they are located are only separated by ~ 0.3 nm. The π - π interaction between these two lobes opens a new transport channel that allows efficient and short-range through-space tunnelling responsible for the observed boost in molecular conductance. To further verify the proposed mechanism, we re-calculated $T(E)$ for the *syn* conformation setting the relevant through-space coupling parameters to zero in its mean-field DFT Hamiltonian (see SI, Figure S7). We found that $T(E)$ for the compressed junction drops by one order of magnitude when only through-bond transmission is allowed, approaching the values found for the relaxed junction. This is further confirmed by a tight-binding model (Figure 4e). Here, a scattering region is weakly coupled to two one-dimensional leads and $T(E)$ increases only as the parameters for through-space coupling β are set to values > 0 .

In conclusion, we present here a novel way to impart mechanosensitivity to molecular junctions, by exploiting a flexible diketone moiety. We found a large increase in conductance upon compression of the junction, and power spectral density analysis combined with density

functional theory calculations demonstrated that mechanosensitivity arises from an *anti* \rightleftharpoons *syn* conformation switch, as the molecule is folded along the flexible bond following junction compression. Non-bonding interactions are increased in the folded *syn* state, allowing through-space charge tunnelling that “shortcuts” a poorly-conductive fragment of the molecule. The switching is reversible and robust, and fabricated junctions can be reliably cycled between high and low conductance states. Our results show the promise of deliberately introducing flexible fragments in otherwise rigid molecular wires, and the fine degree of control on molecular conformation (and hence, charge transport properties) that can be attained in single-molecule junctions.

Experimental Section

Chemicals: compound **1** was synthesized by treating 2 equivalents of 4-bromothioanisole with equimolar *n*-butyllithium, followed by transmetallation to copper (as LiBr adduct) and quench with one equivalent of oxalyl chloride, following the protocol for the preparation of α -diones developed by Babudri *et al.*^[39] The (*E*)-stilbene analogue of **1** (*E*)-1,2-bis(4-(methylthio)phenyl)ethene was synthesized by Wittig olefination of 4-(methylthio)benzaldehyde with 4-(methylthio)benzyltriphenylphosphonium bromide, adapting a literature procedure.^[40] Detailed experimental procedure and characterization data can be found in the SI.

STM-BJ Measurements. Junctions were fabricated and characterised using the *STM-BJ* technique,^[1] using a modified Keysight 5500 STM. Further details on the equipment used, the data acquisition process and its analysis are available in our previous publications on the subject^[19,20] and in the SI.

DFT and Transport Calculations: The optimised geometry, with ground-state Hamiltonian and overlap matrix elements were obtained using DFT and the SIESTA^[41] code. These results were then combined with the Gollum^[38] implementation of the non-equilibrium Green’s function method^[42] to calculate the phase-coherent, elastic-scattering properties of the system, consisting of two gold electrodes and the molecule as scattering region. Further details are available in the SI.

Associated Content

The supporting information is available on the publisher website.

- Synthetic procedures and characterization
- Additional details on STM-BJ measurements
- Control experiments

- Additional details on DFT calculations

Raw single-molecule conductance data acquired for this study and the software used for its analysis are available free of charge on the Research Data Catalogue of the University of Liverpool at the address <http://datacat.liverpool.ac.uk/id/eprint/1038> or at DOI: 10.17638/datacat.liverpool.ac.uk/1038.

Acknowledgments

We thank Prof. Donald Bethell for useful discussion. C.W. acknowledges funding from the China Scholarship Council (grant no. 201806860023). A.V. acknowledges funding from the Royal Society (University Research Fellowship URF\R1\191241) and the School of Physical Sciences of the University of Liverpool (start-up funds and Early Career Researchers grant). S.S. thanks the Leverhulme Trust for funding (Early Career Fellowship ECF-2018-375). H.S. thanks UKRI for funding (Future Leaders Fellowship MR/S015329/1). R.J.N., A.V. and S.J.H. are grateful for financial assistance from the EPSRC (grants EP/M029522/1 and EP/M005046/1).

Notes

The authors declare no competing financial interests.

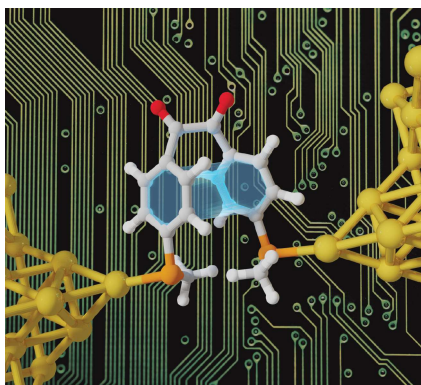
References

- [1] B. Xu, N. Tao, *Science* **2003**, 301, 1221–1223.
- [2] W. Haiss, R. J. Nichols, H. van Zalinge, S. J. Higgins, D. Bethell, D. J. Schiffrin, *Phys. Chem. Chem. Phys.* **2004**, 6, 4330–4337.
- [3] A. Vezzoli, R. J. Brooke, S. J. Higgins, W. Schwarzacher, R. J. Nichols, *Nano Lett.* **2017**, 17, 6702–6707.
- [4] L. Venkataraman, J. E. Klare, I. W. Tam, C. Nuckolls, M. S. Hybertsen, M. L. Steigerwald, *Nano Lett.* **2006**, 6, 458–62.
- [5] J. Zhou, G. Chen, B. Xu, *J. Phys. Chem. C* **2010**, 114, 8587–8592.
- [6] C. R. Arroyo, E. Leary, A. Castellanos-Gómez, G. Rubio-Bollinger, M. T. González, N. Agraït, *J. Am. Chem. Soc.* **2011**, 133, 14313–14319.
- [7] C. Li, I. Pobelov, T. Wandlowski, A. Bagrets, A. Arnold, F. Evers, *J. Am. Chem. Soc.* **2008**, 130, 318–326.
- [8] W. Haiss, H. van Zalinge, D. Bethell, J. Ulstrup, D. J. Schiffrin, R. J. Nichols, *Faraday Discuss.* **2006**, 131, 253–264.
- [9] I. Franco, C. B. George, G. C. Solomon, G. C. Schatz, M. A. Ratner, *J. Am. Chem. Soc.* **2011**, 133, 2242–2249.
- [10] S. T. Schneebeli, M. Kamenetska, Z. Cheng, R. Skouta, R. A. Friesner, L. Venkataraman, R. Breslow, *J. Am. Chem. Soc.* **2011**, 133, 2136–2139.
- [11] M. Bai, J. Liang, L. Xie, S. Sanvito, B. Mao, S. Hou, *J. Chem. Phys.* **2012**, 136, 104701.
- [12] R. Frisenda, V. A. E. C. Janssen, F. C. Grozema, H. S. J. van der Zant, N. Renaud, *Nat. Chem.* **2016**, 8, 1099–1104.
- [13] X. Li, Q. Wu, J. Bai, S. Hou, W. Jiang, C. Tang, H. Song, X. Huang, J. Zheng, Y. Yang, et al., *Angew. Chemie Int. Ed.* **2020**, 59, 3280–3286.
- [14] T. Fu, S. Smith, M. Camarasa-Gómez, X. Yu, J. Xue, C. Nuckolls, F. Evers, L. Venkataraman, S. Wei, *Chem. Sci.* **2019**, 68, 42–61.
- [15] T. Ghane, D. Nozaki, A. Dianat, A. Vladyka, R. Gutierrez, J. P. Chinta, S. Yitzchaik, M. Calame, G. Cuniberti, *J. Phys. Chem. C* **2015**, 119, 6344–6355.
- [16] S. Wu, M. T. González, R. Huber, S. Grunder, M. Mayor, C. Schönenberger, M. Calame, *Nat. Nanotechnol.* **2008**, 3, 569–574.

- [17] S. Martín, I. Grace, M. R. Bryce, C. Wang, R. Jitchati, A. S. Batsanov, S. J. Higgins, C. J. Lambert, R. J. Nichols, *J. Am. Chem. Soc.* **2010**, *132*, 9157–64.
- [18] S. Y. Quek, M. Kamenetska, M. L. Steigerwald, H. J. Choi, S. G. Louie, M. S. Hybertsen, J. B. Neaton, L. Venkataraman, *Nat. Nanotechnol.* **2009**, *4*, 230–234.
- [19] A. K. Ismael, K. Wang, A. Vezzoli, M. K. Al-Khaykanee, H. E. Gallagher, I. M. Grace, C. J. Lambert, B. Xu, R. J. Nichols, S. J. Higgins, *Angew. Chemie Int. Ed.* **2017**, *56*, 15378–15382.
- [20] N. Ferri, N. Algethami, A. Vezzoli, S. Sangtarash, M. McLaughlin, H. Sadeghi, C. J. Lambert, R. J. Nichols, S. J. Higgins, *Angew. Chemie Int. Ed.* **2019**, *58*, 16583–16589.
- [21] M. Taniguchi, M. Tsutsui, K. Yokota, T. Kawai, *Chem. Sci.* **2010**, *1*, 247–253.
- [22] M. Kiguchi, T. Ohto, S. Fujii, K. Sugiyasu, S. Nakajima, M. Takeuchi, H. Nakamura, *J. Am. Chem. Soc.* **2014**, *136*, 7327–32.
- [23] J. S. Meisner, M. Kamenetska, M. Krikorian, M. L. Steigerwald, L. Venkataraman, C. Nuckolls, *Nano Lett.* **2011**, *11*, 1575–1579.
- [24] C. Bruot, J. Hihath, N. Tao, *Nat. Nanotechnol.* **2011**, *7*, 35–40.
- [25] T. a. Su, H. Li, M. L. Steigerwald, L. Venkataraman, C. Nuckolls, *Nat. Chem.* **2015**, *7*, 215–220.
- [26] D. Stefani, K. J. Weiland, M. Skripnik, C. Hsu, M. L. Perrin, M. Mayor, F. Pauly, H. S. J. van der Zant, *Nano Lett.* **2018**, *18*, 5981–5988.
- [27] C. J. Brown, R. Sadanaga, *Acta Crystallogr.* **1965**, *18*, 158–164.
- [28] S. Lopes, A. Gómez-Zavaglia, L. Lapinski, N. Chattopadhyay, R. Fausto, *J. Phys. Chem. A* **2004**, *108*, 8256–8263.
- [29] Z. Pawelka, A. Koll, T. Zeegers-Huyskens, *J. Mol. Struct.* **2001**, *597*, 57–66.
- [30] A. Alanazy, E. Leary, T. Kobatake, S. Sangtarash, M. T. González, H.-W. Jiang, G. R. Bollinger, N. Agrait, H. Sadeghi, I. Grace, et al., *Nanoscale* **2019**, *11*, 13720–13724.
- [31] W. Hong, H. Valkenier, G. Mészáros, D. Z. Manrique, A. Mishchenko, A. Putz, P. M. García, C. J. Lambert, J. C. Hummelen, T. Wandlowski, *Beilstein J. Nanotechnol.* **2011**, *2*, 699–713.
- [32] Y.-P. Zhang, L. Chen, Z.-Q. Zhang, J. Cao, C. Tang, J. Liu, L.-L. Duan, Y. Huo, X. Shao, W. Hong, et al., *J. Am. Chem. Soc.* **2018**, *140*, 6531–6535.

- [33] O. Adak, E. Rosenthal, J. Meisner, E. F. Andrade, A. N. Pasupathy, C. Nuckolls, M. S. Hybertsen, L. Venkataraman, *Nano Lett.* **2015**, *15*, 4143–4149.
- [34] A. Magyarkuti, O. Adak, A. Halbritter, L. Venkataraman, *Nanoscale* **2018**, *10*, 3362–3368.
- [35] C. Tang, L. Chen, L. Zhang, Z. Chen, G. Li, Z. Yan, L. Lin, J. Liu, L. Huang, Y. Ye, et al., *Angew. Chemie Int. Ed.* **2019**, *58*, 10601–10605.
- [36] T. A. Su, H. Li, R. S. Klausen, J. R. Widawsky, A. Batra, M. L. Steigerwald, L. Venkataraman, C. Nuckolls, *J. Am. Chem. Soc.* **2016**, *138*, 7791–7795.
- [37] R. S. Klausen, J. R. Widawsky, M. L. Steigerwald, L. Venkataraman, C. Nuckolls, *J. Am. Chem. Soc.* **2012**, *134*, 4541–4544.
- [38] J. Ferrer, C. J. Lambert, V. M. García-Suárez, D. Z. Manrique, D. Visontai, L. Oroszlany, R. Rodríguez-Ferradás, I. Grace, S. W. D. Bailey, K. Gillemot, et al., *New J. Phys.* **2014**, *16*, 093029.
- [39] F. Babudri, V. Fiandanese, G. Marchese, A. Punzi, *Tetrahedron Lett.* **1995**, *36*, 7305–7308.
- [40] S. V. Aradhya, J. S. Meisner, M. Krikorian, S. Ahn, R. Parameswaran, M. L. Steigerwald, C. Nuckolls, L. Venkataraman, *Nano Lett.* **2012**, *12*, 1643–1647.
- [41] J. M. Soler, E. Artacho, J. D. Gale, A. García, J. Junquera, P. Ordejón, D. Sánchez-Portal, *J. Phys. Condens. Matter* **2002**, *14*, 2745–2779.
- [42] H. Sadeghi, *Nanotechnology* **2018**, *29*, 373001.

Table of Contents



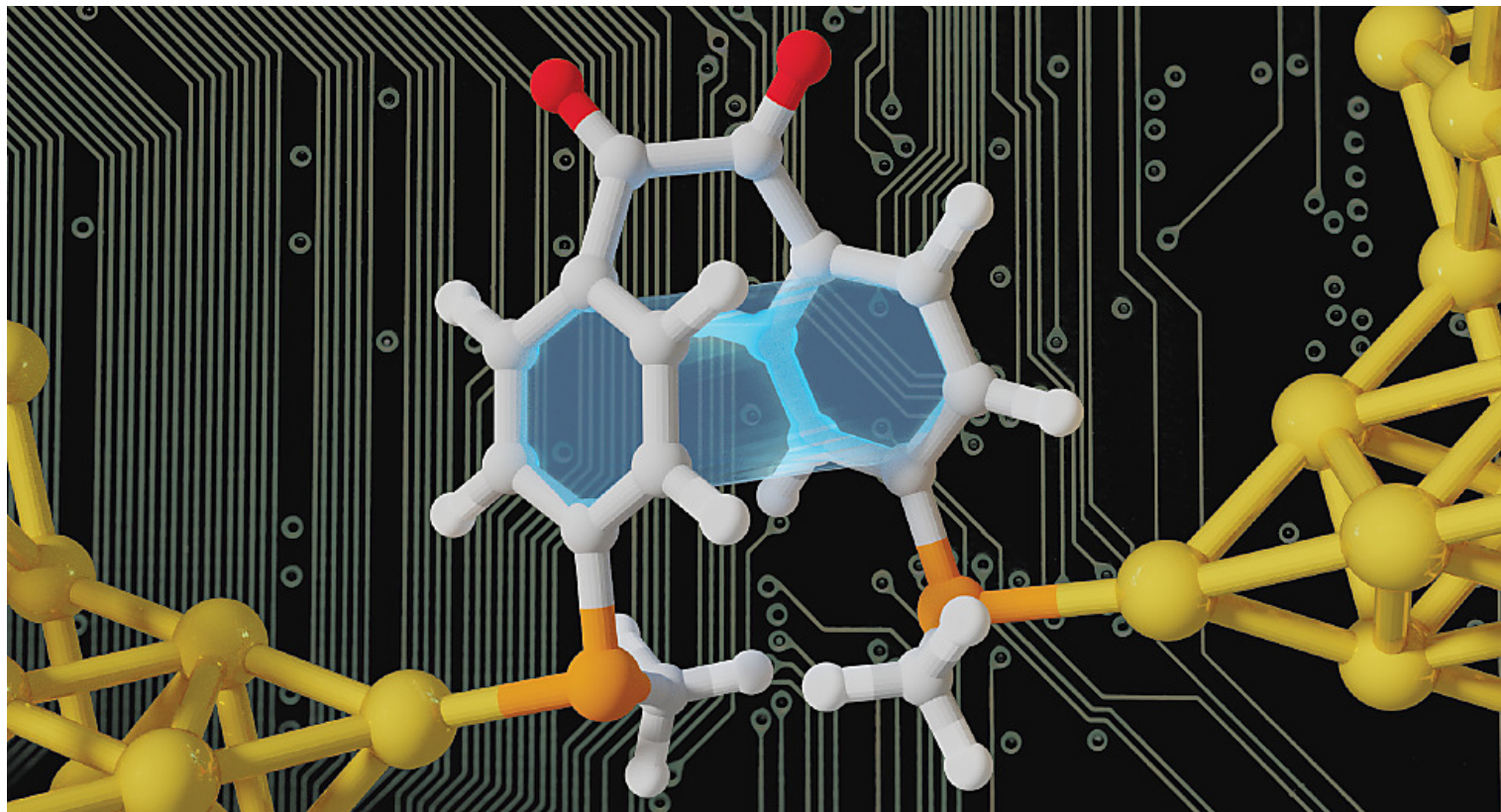
Fold me up: A single-molecule junction that can be mechanically folded around a dicarbonyl bond is presented. In the folded conformation, molecular conductance increases as direct tunnelling between two phenyl fragments of the molecule becomes efficient. The junction can be “unfolded” to its original, thermodynamically stable state simply by pulling the electrodes apart.

Keywords

- Conformational Switching
- Diones
- Ketones
- Mechanoresistivity
- Molecular Devices
- Molecular Electronics
- Nanotechnology

Wu_DKDTSwitch.pdf (1.44 MiB)

[view on ChemRxiv](#) • [download file](#)



Wu_DKDTSwitch_TOC.png (514.71 KiB)

[view on ChemRxiv](#) • [download file](#)

Single-Molecule Junction Origami[†]

Chuanli Wu[‡], Demetris Bates[‡], Sara Sangtarash[‡], Nicolás Ferri, Aidan Thomas, Simon J. Higgins, Craig M. Robertson, Richard J. Nichols, Hatef Sadeghi* and Andrea Vezzoli*

Contents

1. Synthetic Details.....	2
1.1 Synthesis of 1	2
1.2 Synthesis of 4-(methylthio)benzyltriphenylphosphonium bromide	2
1.3 Synthesis of 1,2-bis(4-(methylthio)phenyl)ethene.....	3
2. Details on STM-BJ Data Acquisition and Analysis	4
2.1 Linear Piezo Ramp Experiments	4
2.2 Piezo Modulation Experiments.....	4
2.3 PSD Analysis	5
3. Control Experiments	7
4. Details on DFT and Transport Calculations	9
4.1 Transport Calculations in the absence of π - π interactions	9
4.2 Molecule-electrode electron transfer and position of the LUMO	9
5. Single-Crystal X-Ray crystallographic analysis	11
6. NMR Spectra	14
7. References	18

[†] Ms. Chuanli Wu, Mr. Demetris Bates, Dr. Nicolás Ferri, Mr. Aidan Thomas, Dr. Craig M. Robertson, Prof. Dr. Simon J. Higgins, Prof. Dr. Richard J. Nichols and Dr. Andrea Vezzoli
 Department of Chemistry, University of Liverpool, Crown Street, Liverpool L69 7ZD, United Kingdom
 e-mail for Dr. Andrea Vezzoli: andrea.vezzoli@liverpool.ac.uk

Ms. Chuanli Wu
 School of Chemistry and Materials Science, Nanjing Normal University, Nanjing 210023, People's Republic of China

Dr. Sara Sangtarash and Dr. Hatef Sadeghi
 School of Engineering, University of Warwick, Coventry CV4 7AL, U.K.
 e-mail for Dr. Hatef Sadeghi: hatef.sadeghi@warwick.ac.uk

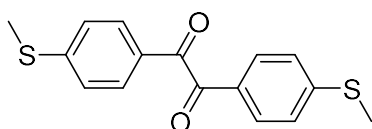
Dr. Andrea Vezzoli
 Stephenson Institute for Renewable Energy, University of Liverpool, Peach Street, Liverpool L69 7ZF, United Kingdom

[‡]: these authors contributed equally to this work.

1. Synthetic Details

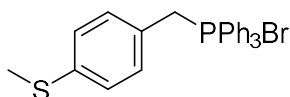
All reactions were carried out under an inert N₂ atmosphere, THF and toluene were dried using an Innovative technology PS-400-6-MD solvent purification system. All other reagents and solvents were purchased from Sigma Aldrich, Acros Organics or Fischer and used as received. Column chromatography was performed on silica gel, monitored by thin layer chromatography (TLC) using Merck silica gel 60 F₂₅₄ plates and visualised under UV light. NMR spectra were recorded on a Bruker Avance III HD and chemical shifts referenced to residual solvent or tetramethylsilane. Mass spectra were recorded by the University of Liverpool Analytical Services on an Agilent QTOF7200 or Agilent QTOF6540 mass spectrometer. Elemental analysis was carried out by The University of Liverpool Analytical Services on an Elementar Vario Micro Cube. Fourier transform infrared (FT-IR) spectra were recorded with a PerkinElmer Spectrum 100 FT-IR spectrometer.

1.1 Synthesis of **1**.



Based on a modified literature procedure.^[1] 4-bromothioanisole (2.00 g, 9.85 mmol) was dissolved in anhydrous THF (50 mL) and cooled to -78 °C. n-Butyllithium (2.5 M, 4.10 mL) was added dropwise and the resulting white suspension (A) was stirred for 1 h. To a second flask was added copper (I) bromide (1.41 g, 9.83 mmol), anhydrous lithium bromide (1.71 g, 19.69 mmol) and anhydrous THF (30 mL), and the mixture (B) was stirred for 10 min before being cooled to -78 °C. The organolithium solution A was added dropwise to B and the mixture was warmed to RT for 5 min before again being cooled to -78 °C, resulting in a yellow solution. To a third flask was added oxalyl chloride (0.41 mL, 4.78 mmol) and anhydrous THF (70 mL). This solution was cooled to -78 °C and the yellow solution (A+B) was added dropwise, and stirred for 3 hr. The resulting yellow solution was then warmed to RT and quenched with sat. NH₄Cl solution (30 mL). The mixture was partitioned between water (40 mL) and ethyl acetate (40 mL) and the organic layer washed with water (3 x 40 mL) and brine (40 mL). All aqueous washings were combined, extracted with CH₂Cl₂ (3 x 40 mL) and the CH₂Cl₂ extracts washed with brine (40 mL). All organic extracts were combined, dried over anhydrous MgSO₄ and the solvent removed under reduced pressure. Yellow needles of pure product were obtained by recrystallisation from ethyl acetate (0.49 g, 34 %): mp: 151-153 °C; IR (cm⁻¹): 3286, 3007, 2926, 1648, 1543, 1552; ¹H NMR (CDCl₃, TMS, 400 MHz): δ = 7.86 (d, 4H, *J* = 8.4 Hz), 7.29 (d, 4H, *J* = 8.4 Hz), 2.53 (s, 6H) ppm; ¹³C{¹H} NMR (CDCl₃, 100 MHz): δ = 193.5, 148.8, 130.2, 129.3, 125.1, 14.6 ppm; Calc. for C₁₆H₁₄O₂S₂: C, 63.55; H, 4.67; S, 21.20. Found: C, 63.44; H, 4.76; S, 20.94. MS (CI⁺): *m/z* 303.1 [M+H]⁺, calc. for C₁₆H₁₅O₂S₂ 303.1.

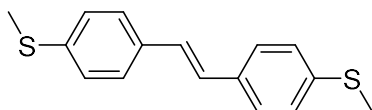
1.2 Synthesis of 4-(methylthio)benzyltriphenylphosphonium bromide



Based on a modified literature procedure.^[2] Triphenylphosphine (0.49 g, 1.87 mmol) was dissolved in anhydrous toluene (5 ml) and heated to reflux. A solution of (4-methylthio)benzyl bromide (0.40 g, 1.84 mmol)

in anhydrous toluene (5 ml) was prepared and added to the refluxing solution. The reaction was cooled after 18 hours and the crude product was collected by filtration. Recrystallisation from CH₂Cl₂/hexane yielded the pure product as a white crystalline solid (0.68 g, 77 %): ¹H NMR (CDCl₃, TMS, 400 MHz): δ = 7.80-7.70 (m, 9H), 7.67-7.59 (m, 6H), 7.07-7.02 (dd, 2H, *J*^{HH} = 8.5 Hz, *J*^{HP} = 2.4 Hz), 6.96 (d, 2H, *J*^{HH} = 8.1 Hz), 5.37 (d, 2H, *J*^{HP} = 14.3 Hz), 2.39 (s, 3H) ppm; ¹³C{¹H} NMR (CDCl₃, 100 MHz): δ = 139.2 (d, *J*^{CP} = 4.5 Hz), 135.0 (d, *J*^{CP} = 2.9 Hz), 134.4 (d, *J*^{CP} = 9.7 Hz), 131.9 (d, *J*^{CP} = 5.7 Hz), 130.1 (d, *J*^{CP} = 12.4 Hz), 126.2 (d, *J*^{CP} = 3.2 Hz), 123.4 (d, *J*^{CP} = 8.9 Hz), 117.8 (d, *J*^{CP} = 85.5 Hz), 30.3 (d, *J*^{CP} = 46.7 Hz), 15.3 ppm; ³¹P{¹H} NMR (162 MHz, CDCl₃): δ = 22.6 ppm; HRMS (ESI⁺): *m/z* 399.1332 [M]⁺, calc. for C₂₆H₂₄PS 399.1331.

1.3 Synthesis of (*E*)-1,2-bis(4-(methylthio)phenyl)ethene



Based on a literature procedure.^[2] Pure (*E*)-1,2-bis(4-(methylthio)phenyl)ethane was obtained as a white powder (0.04 g, 14 %): ¹H NMR (CDCl₃, TMS, 400 MHz): δ = 7.42 (d, 4H, *J* = 8.4 Hz), 7.23 (d, 4H, *J* = 8.4 Hz), 7.01 (s, 2H), 2.50 (s, 6H) ppm; ¹³C{¹H} NMR (CDCl₃, 100 MHz): δ = 137.8, 134.3, 127.4, 126.8, 126.7, 15.9 ppm; HRMS (CI⁺, CH₄): *m/z* 273.0758 [M + H]⁺, calc. for C₁₆H₁₇S₂ 273.0766.

2. Details on STM-BJ Data Acquisition and Analysis

An STM (Keysight Technologies 5500 SPM) equipped with a freshly cut Au tip (Goodfellow Cambridge Au 99.99+%) and a gold-on-mica substrate (200 nm Advent Research Materials Au 99.95% thermally evaporated with an Edwards Auto306 on freshly cleaved on Agar Scientific muscovite mica) was used to fabricate and characterize the molecular junctions. The STM tip position and the tip-substrate bias were controlled by a function generator (Keysight Technologies 33522B) through the STM break-out box (Keysight Technologies N9447A). Measurements were either performed monitoring the current as a function of tip displacement with a home-built 4-channel preamplifier (low-bandwidth, based on the design originally developed by Meszaros *et al.*^[3]), through a USB data acquisition board (NI-9215 - 16-bit @ 10 KSa/s), or by monitoring the current as a function of time with a commercial single-channel transimpedance amplifier (Femto GmbH DLPCA-200), through a PXI system (National Instruments PXIe-1062Q chassis, with a PXIe-4464 DAQ and a PXIe-PCIe8381 interface – 24-bit @ 100 kSa/s). Data acquisition and processing is performed with bespoke software, developed in Labview and Python. In all experiments, the tip is driven into the substrate until the conductance is $> 5G_0$ to ensure the formation of a clean nano-contact, and then retracted with the desired voltage ramp applied to the piezo by more than 6 nm. This ensures that the fabricated junctions are ruptured at the end of the withdrawal cycle. All experiments were performed at 200 mV tip-substrate bias (tip grounded), in a 1 mM mesitylene solution of the target molecular wire. >1000 indentation cycles are performed prior to the introduction of the target solution in order to perform a mechanical annealing of the tip and ensure absence of contamination. For each experiment, >5000 individual traces are collected.

2.1 Linear Piezo Ramp Experiments

All G_z traces collected with a linear piezo ramp (20 nm/s in this study) in the main text and later in this document were used to compile histograms and 2D plots with no further processing or selection.

2.2 Piezo Modulation Experiments

When a non-linear ramp was applied to the piezo to verify the mechanoresistive behavior, a modified protocol was applied. The raw traces, after conversion of current to conductance by using Ohm's law ($G = I/V$) were sliced between abrupt stretches by analysing the second derivative of the signal applied to the piezo transducer and cutting when its value is above a threshold.

The slices were then fed into a sorting algorithm, that takes the average of the first and last modulation and checks that both are below $0.1 G_0$ and above the noise level of the preamplifier ($10^{-5.5} G_0$ at the bias voltage used in this study). This process filters out slices where the tip and the substrate are in contact, those where there is no molecular bridge present and those where the molecular junction did not survive the whole modulation process, leaving only the slices relative to stable molecular junctions. All the slices selected by the sorting algorithm were then used to compile 2D density maps (conductance vs time).

SUPPLEMENTARY INFORMATION

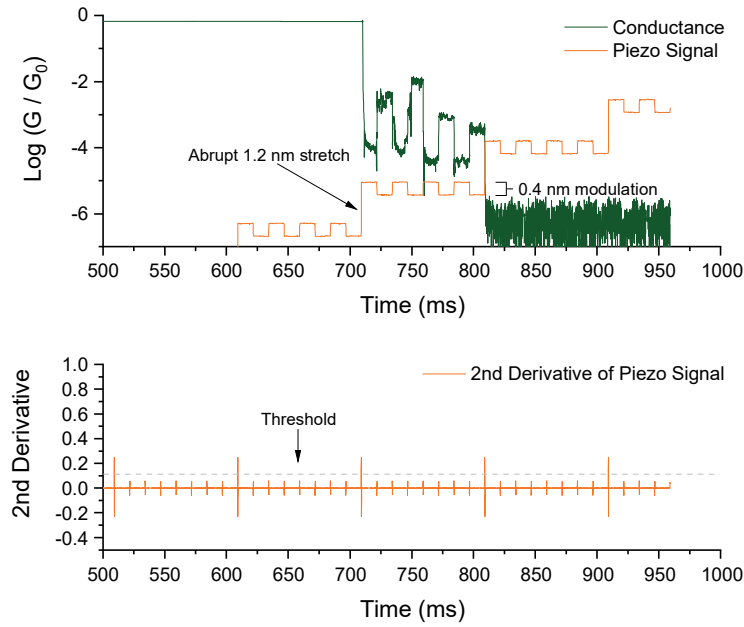


Figure S1: Example of piezo signal and conductance trace (top), and its second derivative (bottom) used in the slicing process.

More details on the process are available in our previous publication on the subject.^[4]

2.3 PSD Analysis

In order to perform PSD analysis on the junction in both its compressed and relaxed state, we performed a measurement with a single modulation cycle, while monitoring current at 100 kSa/s.

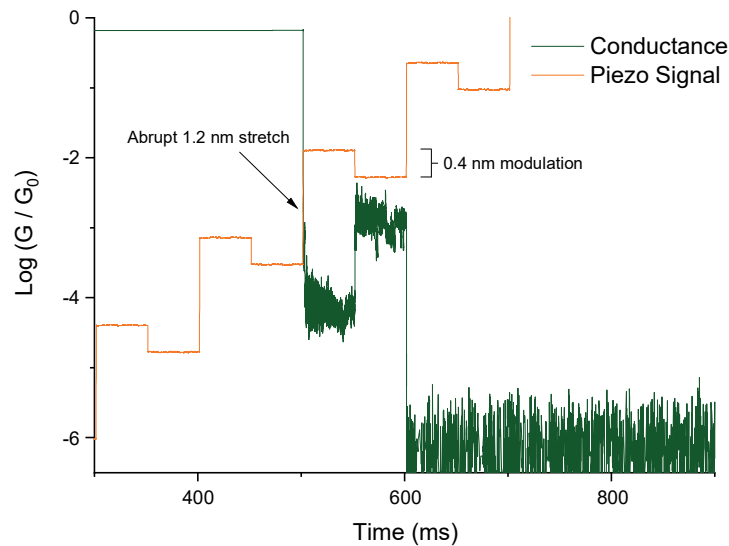


Figure S2: Example of piezo signal and conductance trace (top) for a single-modulation, high frequency data acquisition experiment.

The same algorithm described previously was used to slice and sort conductance traces. Note that the noise floor is higher in this high data acquisition speed experiment, as it scales with \sqrt{Hz} . The individual, single compression cycle slices were separated between the compressed portion and the relaxed one, and each portion was fed to a FFT algorithm (NI Labview2019 Spectral Measurement) with no windowing. We selected

SUPPLEMENTARY INFORMATION

3000 samples in each state to be fed to the FFT algorithm, from the middle of the region of interest, to reduce the influence of piezo creep and sample drift on the measured noise power.

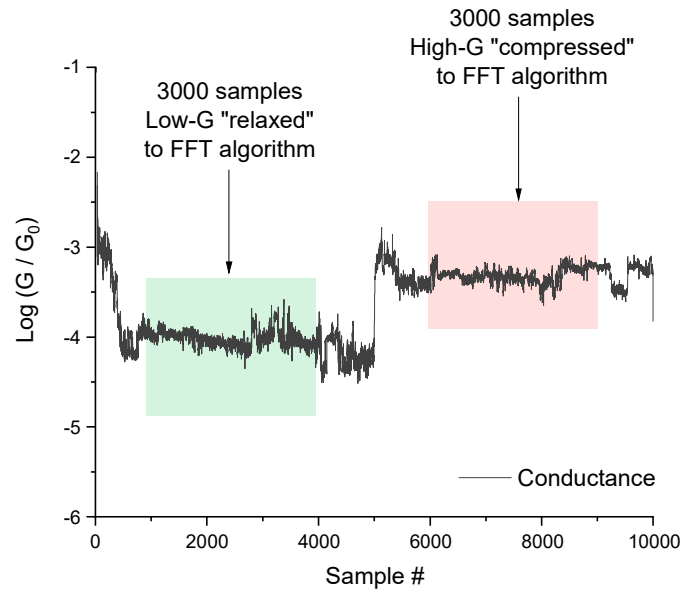


Figure S3 Example single-modulation, high frequency conductance trace with the portion used for PSD analysis highlighted.

The FFT algorithm outputs the *Power Spectral Density* across the whole frequency spectrum. Numerical integration between 100 Hz and 1 kHz yielded the *Noise Power* in this region, that was plotted vs G_{AVG} (average of the conductance of the slice of interest) to give the plots shown in the main paper. The 1 kHz and 100 Hz cut-offs were chosen as they have been demonstrated in the literature to be effective in limiting the contributions to *Noise Power* arising from thermal noise (> 1 kHz) and mechanical vibrations (< 100 Hz).^[5]

3. Control Experiments

As discussed in the main text, we used (*E*)-1,2-bis(4-(methylthio)phenyl)ethene to demonstrate that the switching phenomena do not occur in conformationally-locked compounds.

The synthesis of the compound is described earlier in this document. We started by measuring conductance using a linear ramp, in a regular STM-BJ experiment. No evidence of switching was found, as the results only show a single, sharp and well-resolved peak in the conductance histogram.

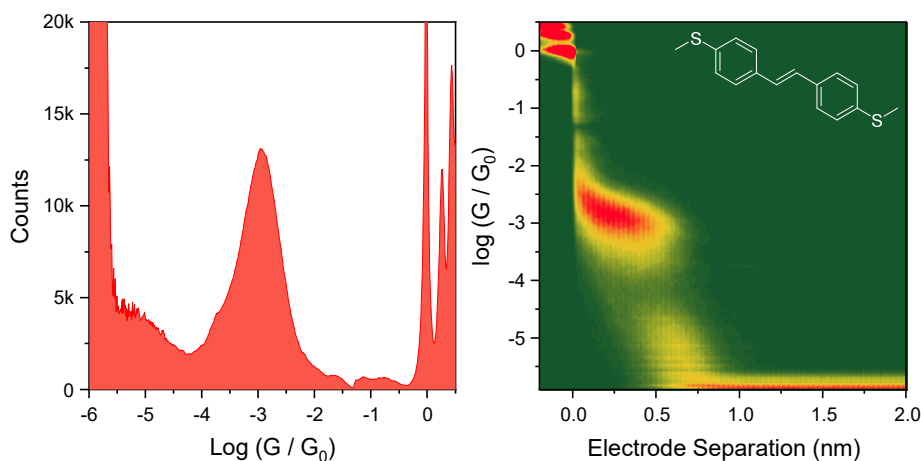


Figure S4: Conductance histogram (left) and 2D density map (right) for 1,2-bis(4-(methylthio)phenyl)ethene (inset). 5841 G_z traces, 200 mV tip-substrate bias.

Similarly, piezo-modulation experiments with the same ramp used for **1**, made of a 1.2 nm abrupt stretch followed by 4 x 0.4 nm modulations, showed only a very shallow increase of conductance upon junction compression.

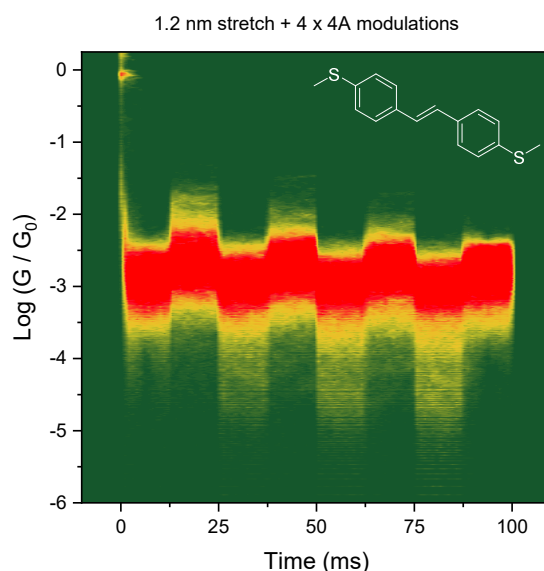


Figure S5: Piezo modulation experiments on 1,2-bis(4-(methylthio)phenyl)ethene (inset). 5022 traces acquired.

We observed a similar behaviour in other, thioanisole-terminated compounds^[4] and we attributed this to an increase in “lateral coupling” – weak interactions between the aromatic π -system and the metallic electrodes already observed in other molecular wires^[6] and clearly not a change in the molecule-electrode binding mode.

SUPPLEMENTARY INFORMATION

Finally, we performed PSD analysis on the traces, to verify the transport pathway in 1,2-bis(4-(methylthio)phenyl)ethene. No correlation between $Noise\ Power / G_{AVG}$ and G_{AVG} was found, thus confirming the molecule has a pure through-bond charge transport mechanism.

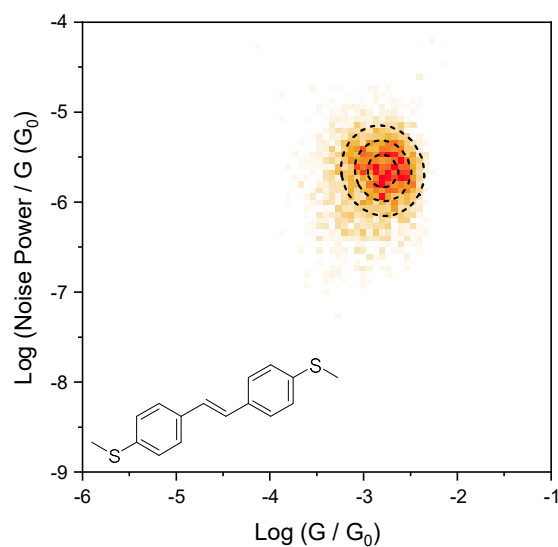


Figure S6: $Noise\ Power / G_{AVG}$ vs G_{AVG} heatmap for 1,2-bis(4-(methylthio)phenyl)ethene. The dashed lines are the contours at 25%, 50% and 75% height of the 2D gaussian fit of the data. 8775 traces.

4. Details on DFT and Transport Calculations

The optimized geometry, ground state Hamiltonian and overlap matrix element of each structure was self-consistently obtained using the SIESTA^[7] implementation of density functional theory (DFT). SIESTA employs norm-conserving pseudo-potentials to account for the core electrons, and linear combinations of atomic orbitals to construct the valence states. The generalized gradient approximation (GGA) of the exchange and correlation functional is used with the Perdew-Burke-Ernzerhof parameterization (PBE) a double- ζ polarized (DZP) basis set, a real-space grid defined with an equivalent energy cut-off of 250 Ry. The geometry optimization for each structure is performed to achieve forces smaller than 10 meV / Å.

The mean-field Hamiltonian obtained from the converged DFT calculation was combined with Gollum^[8] implementation of the non-equilibrium Green's function method^[9] to calculate the phase-coherent, elastic scattering properties of the each system consist of left gold (source) and right gold (drain) leads and the scattering region. The transmission coefficient $T(E)$ for electrons of energy E (passing from the source to the drain) is calculated via the relation: $T(E) = \text{Trace}(\Gamma_R(E)G^R(E)\Gamma_L(E)G^{R\dagger}(E))$. In this expression, $\Gamma_{L,R}(E) = i(\Sigma_{L,R}(E) - \Sigma_{L,R}^\dagger(E))$ describe the level broadening due to the coupling between left (L) and right (R) electrodes and the central scattering region, $\Sigma_{L,R}(E)$ are the retarded self-energies associated with this coupling and $G^R = (ES - H - \Sigma_L - \Sigma_R)^{-1}$ is the retarded Green's function, where H is the Hamiltonian and S is overlap matrix. Using obtained transmission coefficient $T(E)$, the conductance could be calculated by Landauer formula ($G = G_0 \int dE T(E)(-\partial f / \partial E)$) where $G_0 = 2e^2/h$ is conductance quantum.

4.1 Transport Calculations in the absence of π - π interactions

As discussed in the main paper, we performed DFT calculations setting through space coupling parameters to zero, to evaluate the effect of π - π interactions on junction conductance. Results can be found in Figure S7.

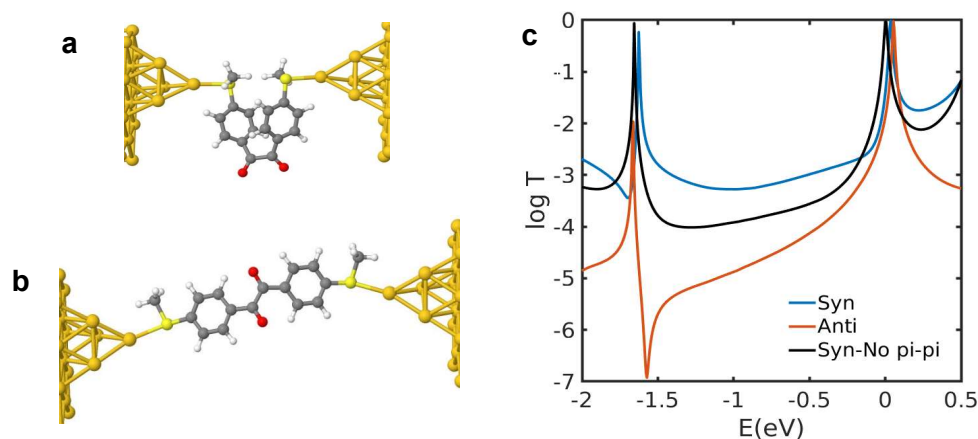


Figure S7: Relaxed structures for the *syn* (a) and *anti* (b) configurations of **1** in the junction. c) Transmission coefficient of the two configurations, and of the *syn* geometry without π - π interactions.

4.2 Molecule-electrode electron transfer and position of the LUMO

In the $T(E)$ curves shown in the main paper, the LUMO resonance of **1** appears to be pinned to the Fermi level of the electrodes. This arises from the strong electron-withdrawing effect of the diketone moiety that induces a strong electrode \rightarrow molecule charge transfer phenomenon. We calculated the LUMO displacement

(Figure S8) and net charge transfer (inset of Figure S8) as a function of the distance between the thiomethyl terminus of **1** and the electrode. As can be seen, up to 0.3 electrons are transferred at the optimal S–Au distance of 2.6 Å, and the LUMO is displaced by up to 20 meV towards the electrodes E_F .

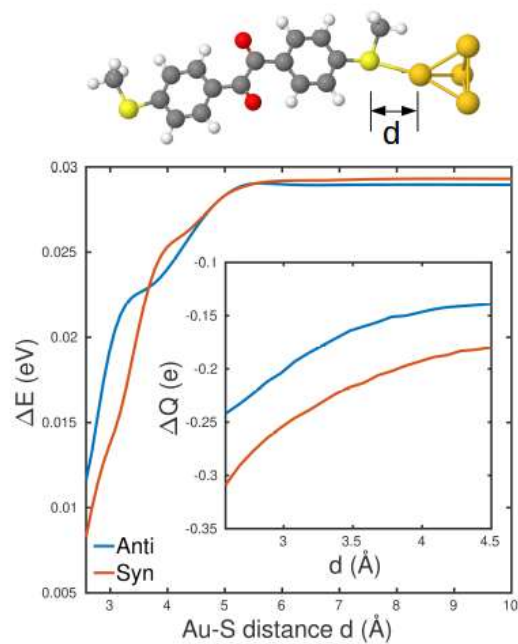


Figure S8: LUMO displacement and net electron transfer (inset) as a function of the S–Au distance d for molecule **1**.

5. Single-Crystal X-Ray crystallographic analysis

Yellow needles of **1** were grown by recrystallisation of the crude material from ethyl acetate/CH₂Cl₂. Clear platelets of **(E)-1,2-bis(4-(methylthio)phenyl)ethene** were grown by dissolution in hot acetonitrile followed by evaporation. Crystals were mounted on a MiTeGen MicroMount using Parabar oil. X-ray data were collected at 150 K using Mo-K α (λ = 0.71073) for **1** and Cu-K α radiation (λ = 1.54178 Å) for **(E)-1,2-bis(4-(methylthio)phenyl)ethene** on a Bruker Venture D8 dual-source micro-focus diffractometer fitted with a Photon 100 CMOS detector using φ and ω scans. Integration and reduction were undertaken with Apex 3 software (Bruker AXS Inc.). Subsequent computations were employed using the OLEX2 software interface.^[10] Absorption corrections were applied to the data using SADABS (Bruker AXS Inc.). Structures were solved via direct methods using SHELXT^[11] followed by refinement with SHELXL.^[12] Non-hydrogen atoms were refined anisotropically.

	1	1,2-bis(4-(methylthio)phenyl)ethene
CCDC Number	1950830	1988159
Empirical formula	C ₁₆ H ₁₄ O ₂ S ₂	C ₁₆ H ₁₆ S ₂
Formula weight	302.39	272.41
Temperature/K	150.0	150.02
Crystal system	Monoclinic	Monoclinic
Space group	<i>C2/c</i>	<i>P2₁/c</i>
<i>a</i> /Å	23.463(3)	5.6118(2)
<i>b</i> /Å	4.0517(5)	7.2767(3)
<i>c</i> /Å	15.524(2)	33.6777(13)
α /°	90	90
β /°	106.312(6)	93.1630(10)
γ /°	90	90
Volume/Å ³	1416.3(3)	1373.15(9)
<i>Z</i>	4	4
ρ_{calc} g/cm ³	1.418	1.318
μ /mm ⁻¹	0.373	3.318
<i>F</i> (000)	632.0	576.0
Crystal size/mm ³	0.2 × 0.08 × 0.04	0.2 × 0.2 × 0.06
Radiation/ Å	0.71073	1.54178
2 θ range for data collection/°	5.468 to 52.858	5.256 to 133.378
Index ranges	-28 ≤ <i>h</i> ≤ 28, -5 ≤ <i>k</i> ≤ 5, -19 ≤ <i>l</i> ≤ 19	-6 ≤ <i>h</i> ≤ 6, -7 ≤ <i>k</i> ≤ 8, -39 ≤ <i>l</i> ≤ 40
Reflections collected	6486	16702
Independent reflections	1440 [<i>R</i> _{int} = 0.0591, <i>R</i> _{sigma} = 0.0332]	2419 [<i>R</i> _{int} = 0.0282, <i>R</i> _{sigma} = 0.0177]
Data/restraints/parameters	1440/0/92	2419/0/165
Goodness-of-fit on <i>F</i> ²	1.177	1.060
Final <i>R</i> indexes [<i>I</i> ≥ 2 σ (<i>I</i>)]	<i>R</i> ₁ = 0.0438 <i>wR</i> ₂ = 0.1079	<i>R</i> ₁ = 0.0253 <i>wR</i> ₂ = 0.0664
Final <i>R</i> indexes [all data]	<i>R</i> ₁ = 0.0539 <i>wR</i> ₂ = 0.1137	<i>R</i> ₁ = 0.0286 <i>wR</i> ₂ = 0.0683
Largest diff. peak/hole / e Å ⁻³	0.38/-0.35	0.22/-0.20

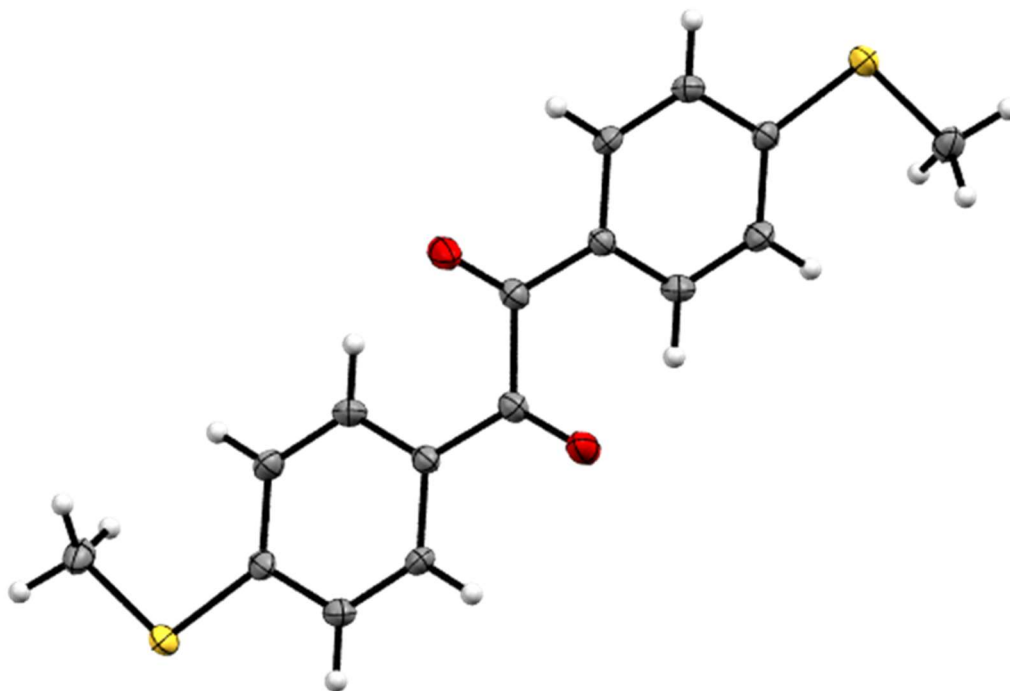


Figure S9: Crystal structure of **1**. Thermal ellipsoids are drawn at 50% probability.

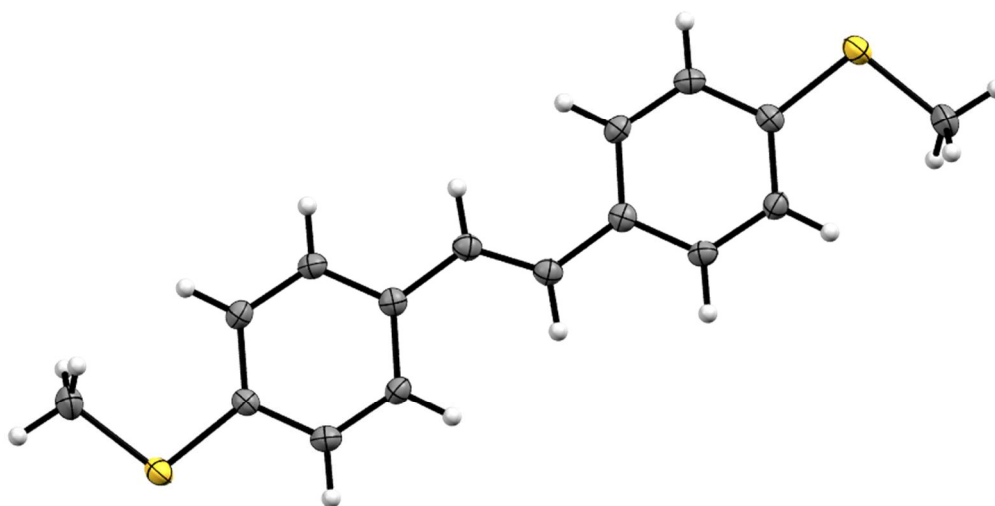


Figure S10: Crystal structure of 1,2-bis(4-(methylthio)phenyl)ethane. Thermal ellipsoids are drawn at 50% probability.

Colours used for crystallographic figures: carbon – grey, hydrogen – white, oxygen – red, sulphur – yellow.

SUPPLEMENTARY INFORMATION

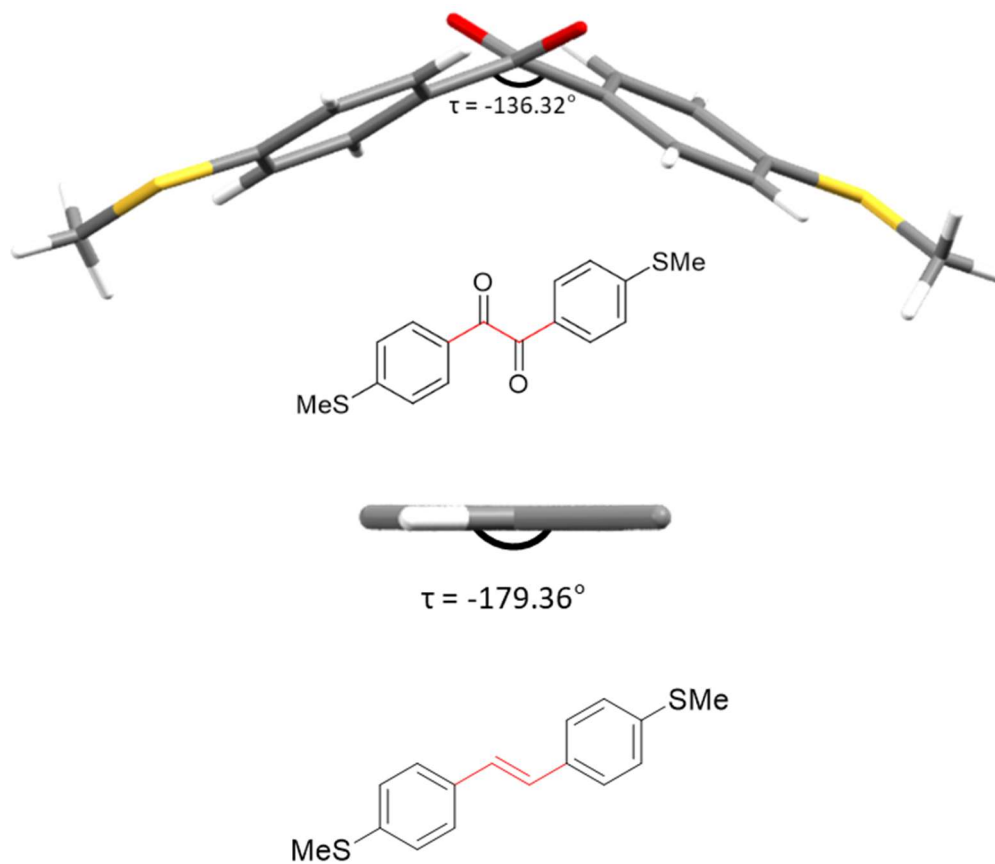


Figure S11: (top) View along central C-C bond of **1** with dihedral angle (τ) displayed. (bottom) View along central C=C bond of 1,2-bis(4-(methylthio)phenyl)ethane with τ displayed. Aromatic rings are omitted for clarity. τ is defined for the bonds highlighted in red for each structure.

6. NMR Spectra

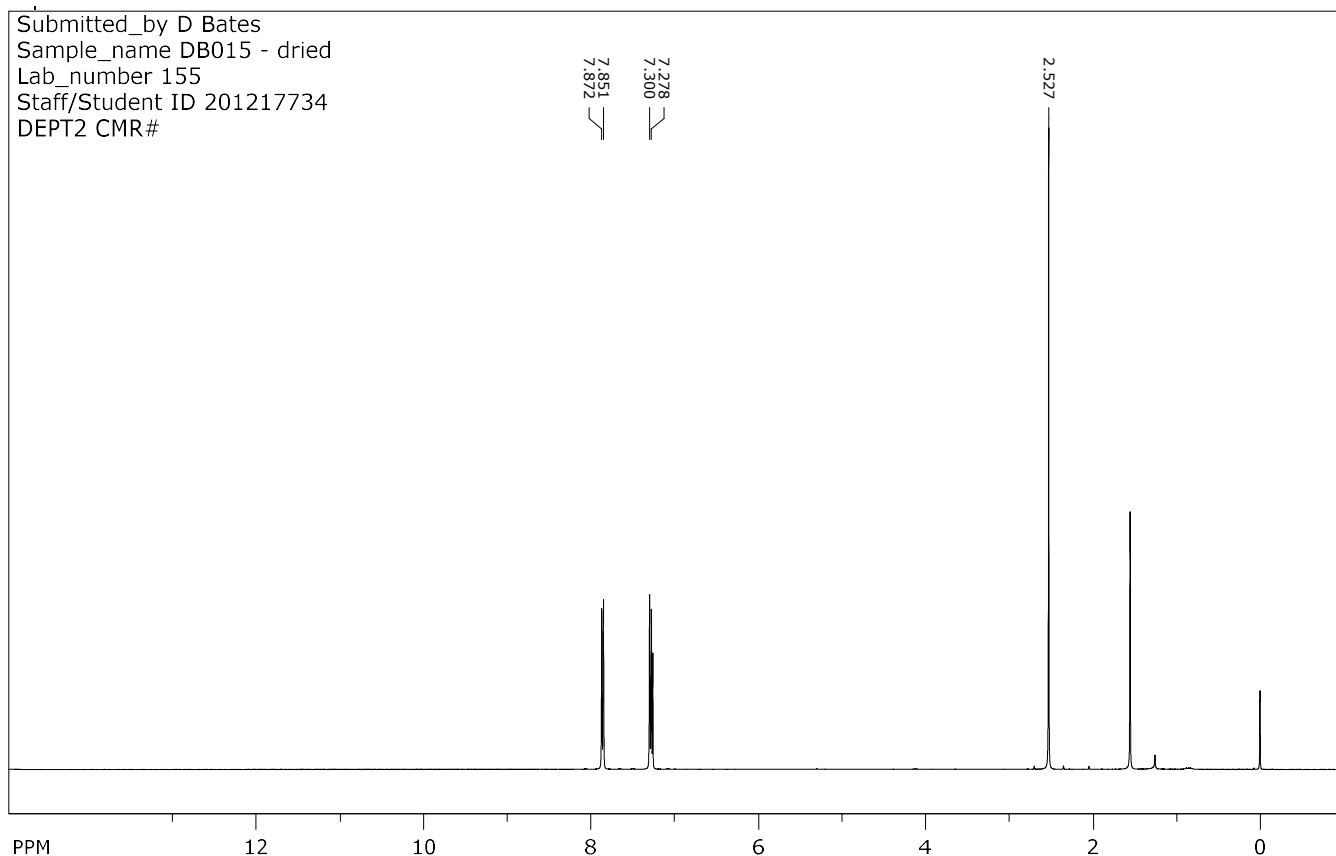


Figure S12 : ^1H NMR spectrum for **1**.
Residual solvent peaks: 1.27: petroleum ether; 1.55: water; 7.26 ppm: chloroform.

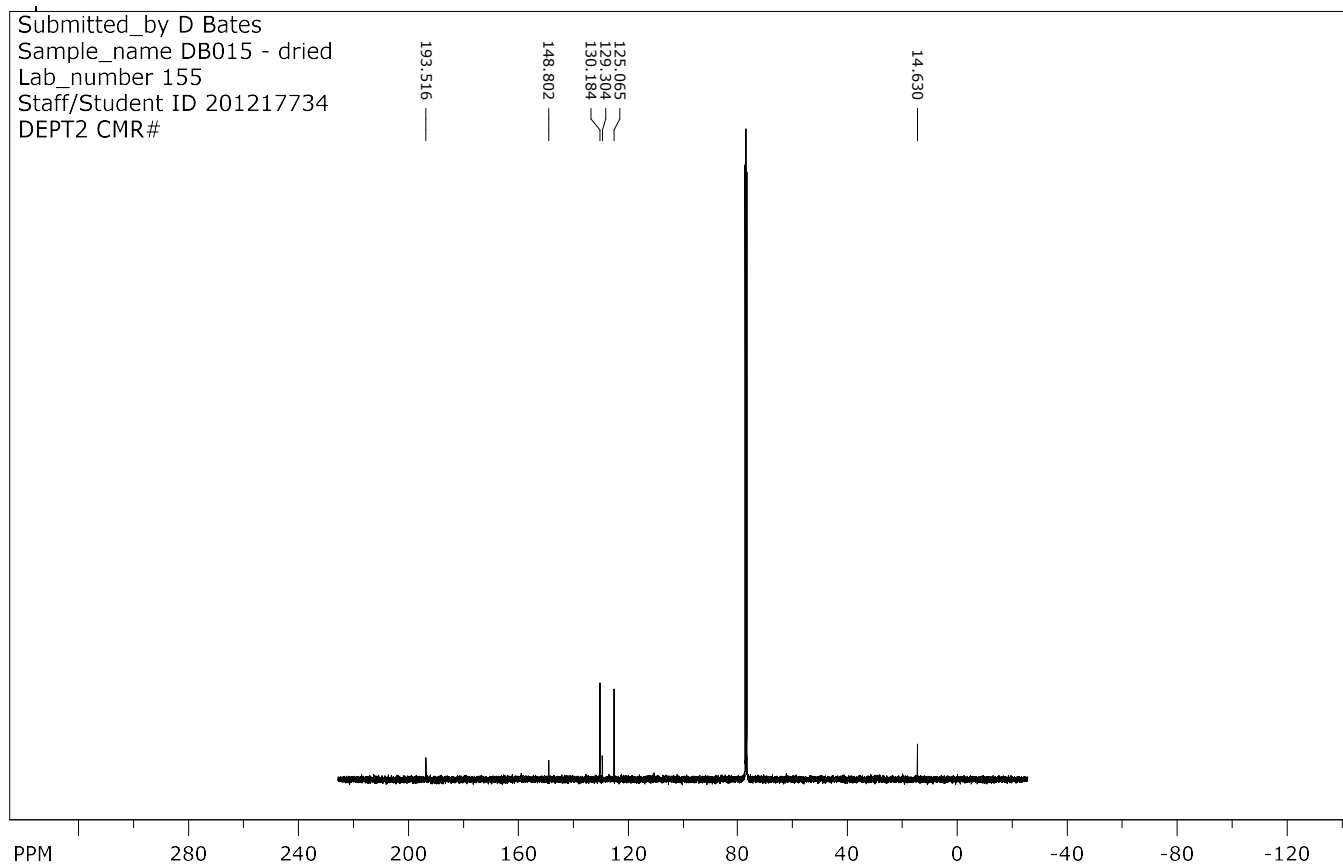


Figure S13 : ^{13}C NMR spectrum for **1**.

SUPPLEMENTARY INFORMATION

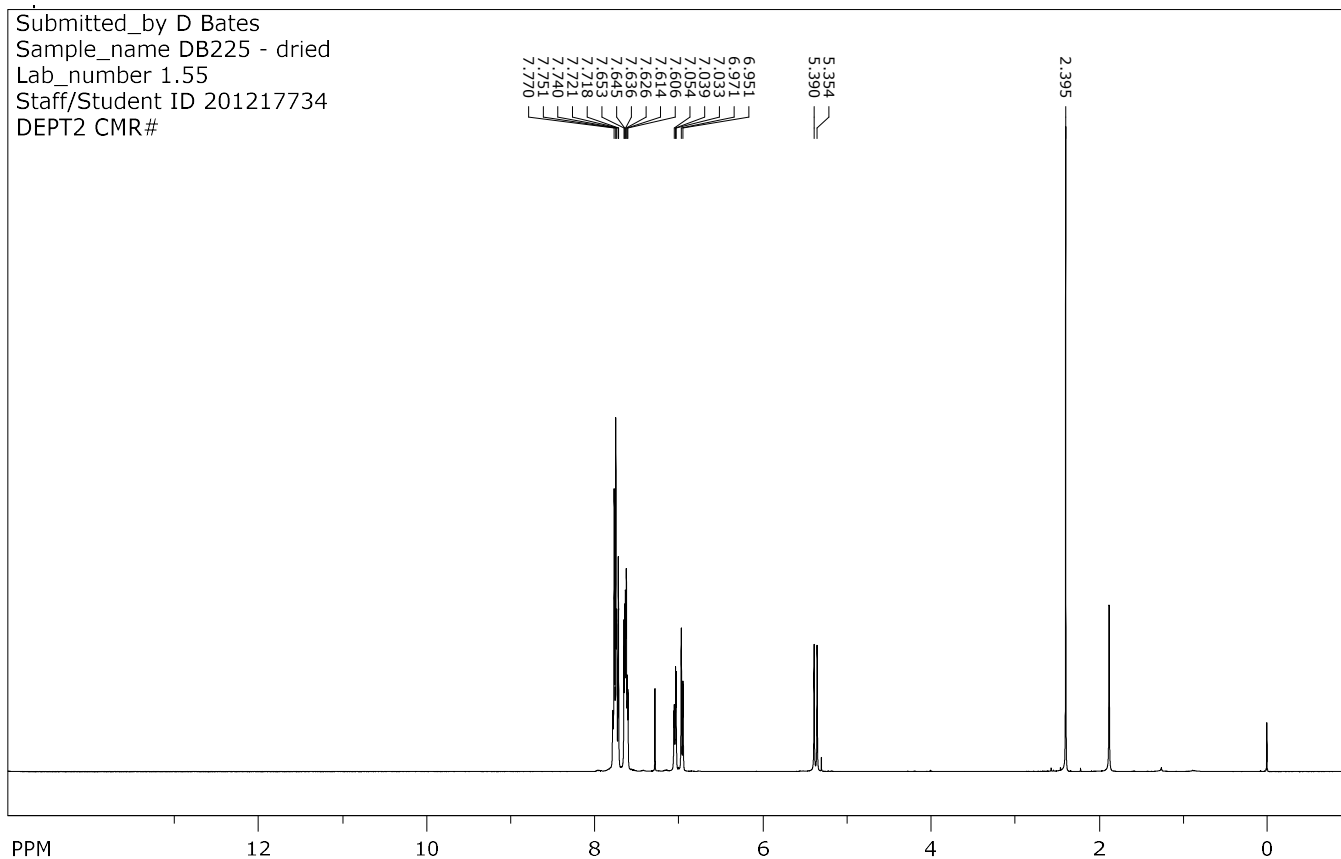


Figure S14 : ^1H NMR spectrum for 4-(methylthio)benzyltriphenylphosphonium bromide.
Residual solvent peaks: 1.88: water; 5.40: CH_2Cl_2 ; 7.28 ppm: chloroform.

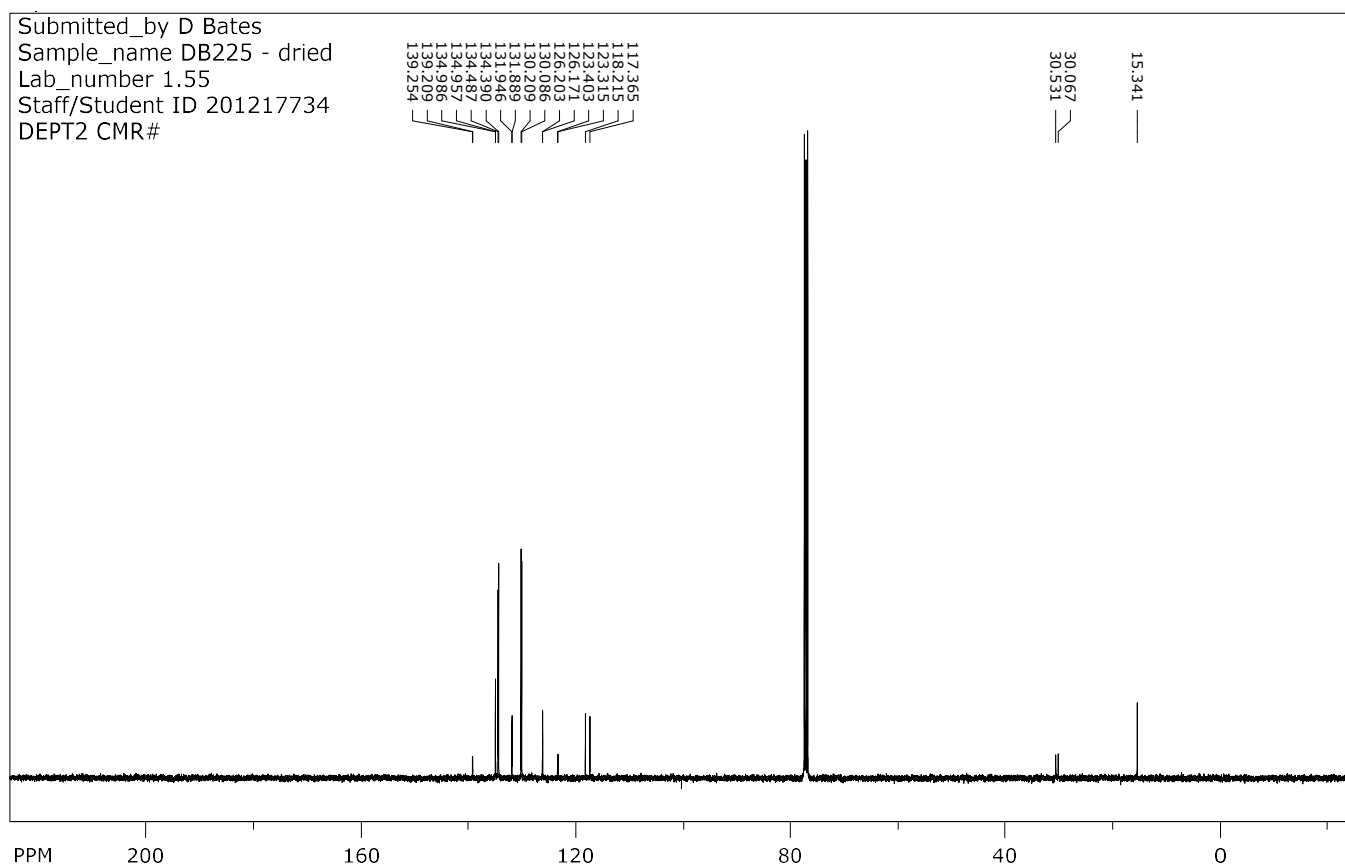


Figure S15 : ^{13}C NMR spectrum for 4-(methylthio)benzyltriphenylphosphonium bromide.

SUPPLEMENTARY INFORMATION

Submitted_by D Bates
Sample_name DB225 - dried
Lab_number 1.55
Staff/Student ID 201217734
DEPT2 CMR#

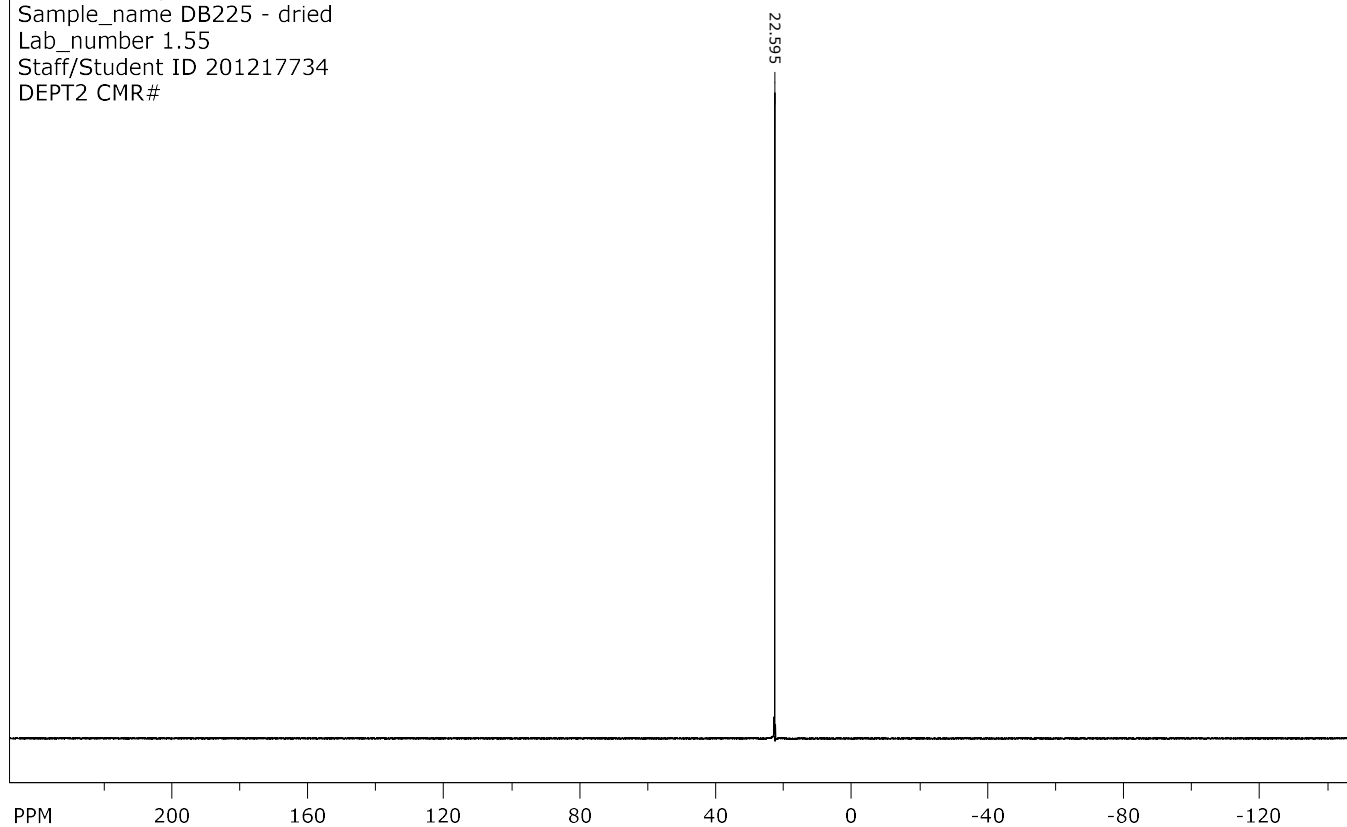


Figure S16 : ^{31}P NMR spectrum for 4-(methylthio)benzyltriphenylphosphonium bromide.

Submitted_by D Bates
Sample_name DB226 - dried
Lab_number 1.55
Staff/Student ID 201217734
DEPT2 CMR#

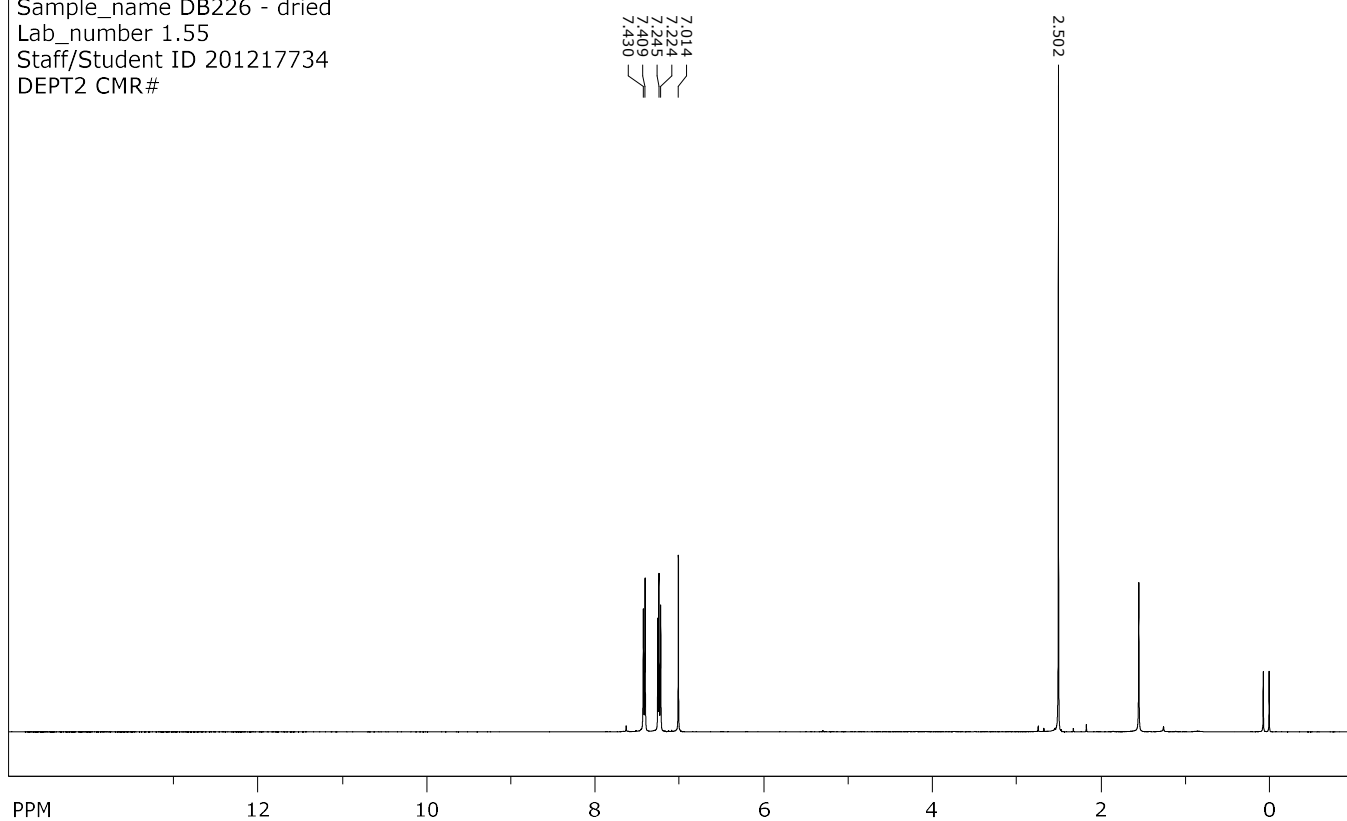


Figure S17 : ^1H NMR spectrum for (E)-1,2-bis(4-(methylthio)phenyl)ethane.
Residual solvent peaks: 0.07: silicon grease; 1.55: water; 7.26 ppm: chloroform.

SUPPLEMENTARY INFORMATION

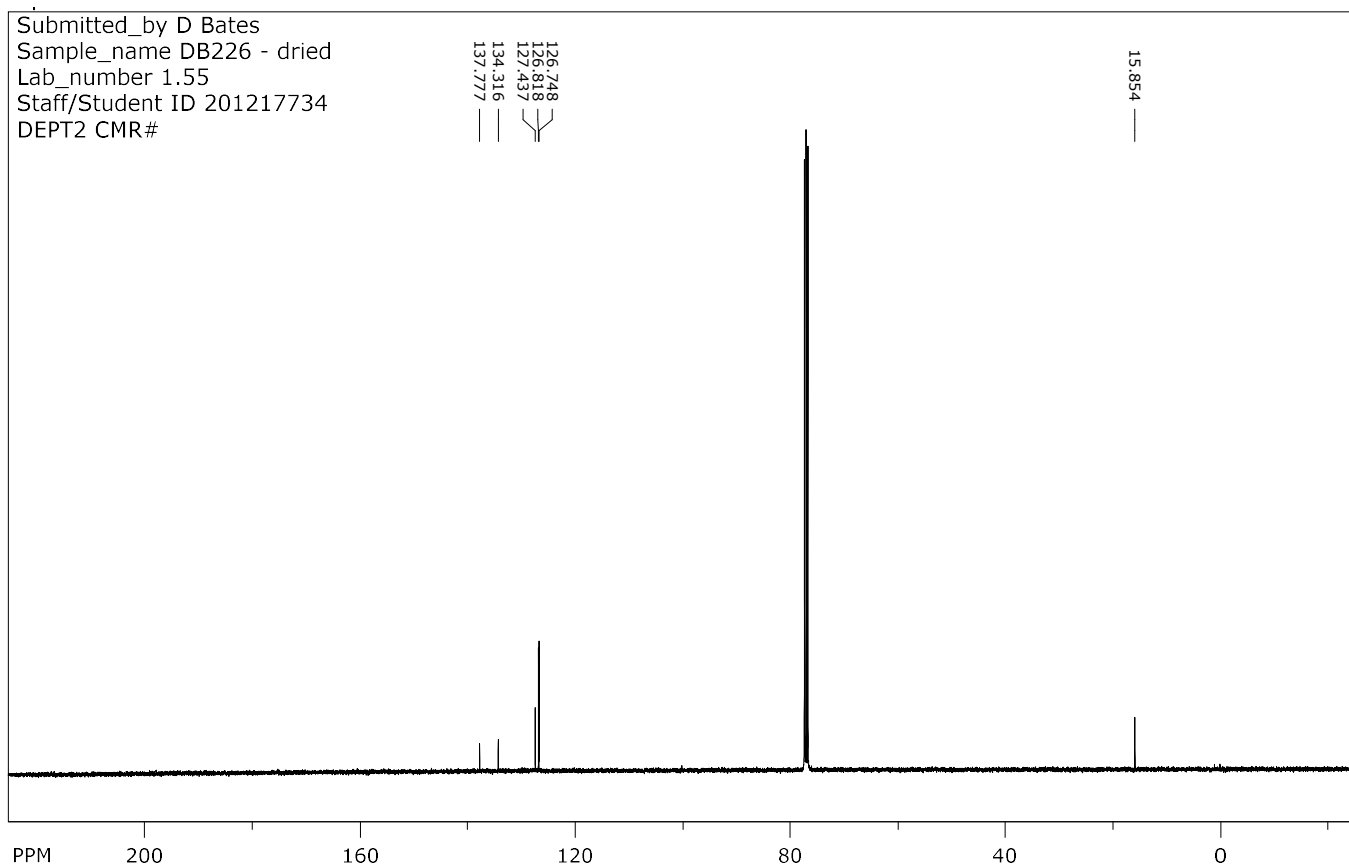


Figure S18 : ^{13}C NMR spectrum for (E)-1,2-bis(4-(methylthio)phenyl)ethane.

7. References

- [1] F. a. Arroyave, C. a. Richard, J. R. Reynolds, *Org. Lett.* **2012**, *14*, 6138–6141.
- [2] S. V. Aradhya, J. S. Meisner, M. Krikorian, S. Ahn, R. Parameswaran, M. L. Steigerwald, C. Nuckolls, L. Venkataraman, *Nano Lett.* **2012**, *12*, 1643–1647.
- [3] G. Mészáros, C. Li, I. Pobelov, T. Wandlowski, *Nanotechnology* **2007**, *18*, 424004.
- [4] N. Ferri, N. Algethami, A. Vezzoli, S. Sangtarash, M. McLaughlin, H. Sadeghi, C. J. Lambert, R. J. Nichols, S. J. Higgins, *Angew. Chemie Int. Ed.* **2019**, *58*, 16583–16589.
- [5] O. Adak, E. Rosenthal, J. Meisner, E. F. Andrade, A. N. Pasupathy, C. Nuckolls, M. S. Hybertsen, L. Venkataraman, *Nano Lett.* **2015**, *15*, 4143–4149.
- [6] I. Diez-Perez, J. Hihath, T. Hines, Z.-S. Wang, G. Zhou, K. Müllen, N. Tao, *Nat. Nanotechnol.* **2011**, *6*, 226–231.
- [7] J. M. Soler, E. Artacho, J. D. Gale, A. García, J. Junquera, P. Ordejón, D. Sánchez-Portal, *J. Phys. Condens. Matter* **2002**, *14*, 2745–2779.
- [8] J. Ferrer, C. J. Lambert, V. M. García-Suárez, D. Z. Manrique, D. Visontai, L. Oroszlany, R. Rodríguez-Ferradás, I. Grace, S. W. D. Bailey, K. Gillemot, et al., *New J. Phys.* **2014**, *16*, 093029.
- [9] H. Sadeghi, *Nanotechnology* **2018**, *29*, 373001.
- [10] O. V. Dolomanov, L. J. Bourhis, R. J. Gildea, J. A. K. Howard, H. Puschmann, *J. Appl. Crystallogr.* **2009**, *42*, 339–341.
- [11] G. M. Sheldrick, *Acta Crystallogr. Sect. A Found. Crystallogr.* **2015**, *71*, 3–8.
- [12] G. M. Sheldrick, *Acta Crystallogr. Sect. C Struct. Chem.* **2015**, *71*, 3–8.

Wu_DKDTSwitch_SI.pdf (2.47 MiB)

[view on ChemRxiv](#) • [download file](#)
